Production and characterization of thin a-C:(H) films for gas permeation barrier functionality against He, CO_2, N_2, O_2 and H_2O

2006 J. Phys.: Condens. Matter 18 5945

(http://iopscience.iop.org/0953-8984/18/26/014)

INSTITUTE OF PHYSICS PUBLISHING JOURNAL OF PHYSICS: CONDENSED MATTER

J. Phys.: Condens. Matter **18** (2006) 5945–5959 doi:10.1088/0953-8984/18/26/014

Production and characterization of thin a-C:(H) films for gas permeation barrier functionality against He, CO_2, N_2, O_2 and H_2O

N Laidani[1,3], R Bartali[1], G Gottardi[1], M Anderle[1], G Chuste[2,4] and C Bellachioma[2,5]

[1] ITC-IRST, Divisione Fisica-Chimica delle Superfici ed Interfacce, Via Sommarive, 18, 38050 Povo (Trento), Italy
[2] CERN, TS/MME/SC, Meyrin, 1211, Geneva, Switzerland

E-mail: laidani@itc.it

Received 23 February 2006
Published 16 June 2006
Online at stacks.iop.org/JPhysCM/18/5945

Abstract

This work reports on (i) the gas barrier properties of a-C:H films rf-sputtered in Ar–H_2 plasmas from a graphite target on polyethylene terephthalate (PET) and (ii) the influence of the film chemical structure and defect properties on the gas permeability. The intrinsic permeabilities of the films to He, CO_2, O_2, N_2 gases and H_2O vapour were determined and found to be orders of magnitude lower than that of the bare PET. Indirect evidence was given to a solubility–diffusion process as the more probable permeation mechanism, over a gas flow through microdefects or gas transport through nanodefects by a Knudsen diffusion mechanism. The barrier capability of the films was found to scale as the gas molecular diameter within the He, CO_2, O_2 and N_2 series, and inversely with the gas critical temperature for the CO_2, O_2, N_2 and H_2O series. A correlation between the film Urbach energy, E_u, and the gas permeability was established, except for H_2O. Such findings further favour a bulk diffusion contributing mechanism to permeation over the gas state transport. Conversely, this E_u-permeability relation shed more light on the origin of the valence band tailing of the amorphous carbon electron structure.

(Some figures in this article are in colour only in the electronic version)

[3] Author to whom any correspondence should be addressed.
[4] Present address: Thalès Electronics, Thonon-les-Bains, France.
[5] Present address: GSI-Gesellschaft für Schwerionenforschung Abt. VBE/UHV, Planckstrasse 1-64291 Darmstadt, Germany.

1. Introduction

The field of gas barrier applications is broad and covers food and pharmaceutical packaging, medical supplies and hermetic seals over integrated circuits in microelectronics or devices such as OLEDs. In parallel, there is an ever increasing need for eco-efficient and recyclable functional materials, a need also dictated by legislation. Non-metallic materials such as transparent oxides of Al, Si and Mg have been investigated for gas barrier applications [1–4]. They also meet ecological demands but their application is rather limited by their low mechanical stability. Carbon-based organic films, due to a combination of many useful properties, are materials of great potential whenever a resistance to mechanical loads is required together with a gas barrier capability. In this frame, carbon films deposited on plastic substrates have been the subject of many recent studies [5–9].

In a previous work, the authors established a correlation between the plasma process parameters used for a-C:H film deposition on polyethylene terephthalate (PET) and the permeation properties of the a-C:H/PET system to He gas [10]. This study was further pursued in order to determine the intrinsic permeability of the films in relation with their structural properties. Conversely, the film behaviour concerning gas permeation provided qualitative information for a better network structure understanding. The findings of this work are presented in this paper, which is organized as follows. The results of a film growth study will be given first, then the film permeation behaviour and structural properties and finally the correlations between the permeability characteristics and the defect-related disorder.

2. Experimental details

2.1. Film deposition

The carbon films were sputter-deposited from graphite in 5 Pa rf (13.56 MHz) discharges in an Ar–H_2 mixture containing (0–84)% H_2 flowing at 30 sccm. The substrates were mounted on a water-cooled rotating support and at a distance of 8 cm from the cathode. The different film C/H atomic ratios and network structures were achieved either through the feedgas composition variation when a continuous wave (CW) rf plasma was created [11], or through the modulation of the rf discharge for a given feedgas composition [10]. The films are designated as a-C:H(x) where x identifies the percentage of hydrogen used in the Ar–H_2 feedgas.

The discharge modulation was achieved by pulsing with 1–100 kHz frequencies. For the CW plasmas, a constant cathode dc self-bias of −550 V was maintained. The modulated discharges were also produced with −550 V discharge voltage either during the 'time on' of the pulse with a 0 V 'time off' value, or as an average over the 'on' and the 'off' times of the pulse. As the present work focuses only on the film structure–permeability correlations, no weight is directly given to the process parameter effects themselves on the film structure.

Aluminium films, from 60 nm to ∼1 μm thick, were also deposited on PET by sputtering of an Al target in pure argon, and these served as references for the gas permeation tests [10].

PET membranes (125 and 175 μm thick) and n-type Si(100) were used as substrates. They were cleaned in ultrasonic baths in isopropanol. Series of samples were prepared with film thicknesses from 10 to ∼500 nm.

A polymer-like carbon film was also deposited on Si(100) by plasma-assisted chemical vapour deposition (PACVD) in the same apparatus and using CH_4–N_2–H_2 (10–60–30% respectively) as precursor. Later, films were grown on it with different thicknesses by graphite sputtering in Ar–H_2 as above. These pre-coated Si substrates were used in order to simulate the growth mechanism of the a-C:H films of this study on a polymeric substrate such as PET.

2.2. Film characterization

(a) Thickness, mass density and stress measurements. The film thickness and the internal stress were measured with a Kla Tencor P15 profilometer. The internal stress was calculated with Stoney's equation: $\sigma = [E_s \times l_s/6(1-\nu_s) \times l_f]\,(1/r - 1/r_0)$, with $E_s/6(1-\nu_s) = 1.805 \times 10^{11}$ Pa being the biaxial modulus of the Si(100) substrate, l_s and l_f the substrate and film thickness respectively, and r and r_0 the substrate curvature radius after and before deposition. The substrate weight uptake upon coating was measured with a 1×10^{-5} g precision for film mass density calculation.

(b) Chemical and morphological characterization. Fourier-transform infra-red spectroscopy (FT-IR) was used to semi-quantify the chemically bound hydrogen content of the films. It was carried out with a Bio-Rad FTS 185 spectrometer equipped with a DTGS detector and a KBr beam splitter, in the absorbance mode and in the 400–4000 cm^{-1} wavenumber range. In particular, the 2600–3200 cm^{-1} interval was considered, corresponding to the stretching vibration modes of various C–H bonds [12]; and this allowed us to determine the composition of the hydrogenated phase. The integrated absorbance $\int \frac{A(\omega)}{l_f \times \omega}\,d\omega$ was calculated over the whole band, $A(\omega)$ being the absorbance at wavenumber ω and l_f the film thickness [13].

The film surface morphology was investigated by optical microscopy with back illumination of the coated PET sample.

(c) Optical characterization. Optical transmittance (T) and reflectance (R) measurements were made with a Jasco V-550 spectrophotometer in the 200–800 nm wavelength range at normal light incidence, to determine the film absorption coefficient α, the Tauc gap and Urbach energies [14, 15], as well as the refractive index (n). The latter was determined from the R expression for an absorbing medium of index (n, k) [16].

(d) Gas permeation tests. The permeation tests with He, CO_2, N_2, O_2 and H_2O were carried out by two methods: a dynamic one and an accumulation one. The first test group was performed in a vacuum system split into two chambers by the sample itself, both pre-pumped to below 10^{-7} Torr and then valved-off on one side of the sample. In the latter chamber the gas was injected for permeation measurements, at about a 100 Torr pressure, recorded by a capacitance gauge (Balzers CMR 261). With this system configuration, a residual gas analyser (Balzers QMA-125) followed the partial pressure evolution of the permeant gas in the low pressure side. The permeability (P) can then be derived from the pressure ratio on the both sides of the membrane (low and high pressures, p_l and p_h respectively, with $p_l \ll p_h$), the pumping speed (s) on the low-pressure side, the membrane area (A) and thickness (l) following:

$$P = \frac{p_l}{p_h} \times \frac{S \times l}{A}. \tag{1}$$

This method was essentially used for the permeation tests with He.

Tests with the other gases (CO_2, N_2, O_2, H_2O) were made with the second method, based on the pressure accumulation in a closed volume, $V = 38.5$ cm^3. The gas, injected with a pressure up to 760 Torr, was allowed to permeate through the membrane from the p_h side to the p_l side, but in this case, the latter volume was closed. The pressure increase in this volume was monitored by a capacitive gauge. In such a measurement the permeability, P, is directly proportional to the slope of the straight line representing the gas accumulation as a function of time in the steady-state regime, after an accurate pressure background subtraction, as

$$P = \frac{V \times l}{A \times p_h} \times \text{slope}. \tag{2}$$

In contrast with the dynamic method, the permeation measurements were achieved at the same time on both the coated membrane and the bare membrane, in two parallel systems, to avoid

external condition fluctuations which would be deleterious to the measurement precision in the case of slow permeation rates. This was why this procedure was preferred over the first one for the tests with CO_2, N_2, O_2, and H_2O. Permeance (or transmission rate) is defined as $Q = \frac{P}{l}$. The measurement repeatability, determined on bare PET membranes and on some of the coated ones, was within 10–20%.

3. Results and discussion

3.1. Background and early results

A study of the chemical role of hydrogen in the target erosion in an Ar–H_2 plasma used to grow amorphous carbon films from graphite showed evidence of two regimes: a reactive sputtering (i.e. physical sputtering of a hydrogenated target) and an essentially chemical erosion [11]. The first mechanism operated in plasmas created with the H_2-poorest feedgas (3–20% H_2) while the second described better the target erosion for the remaining concentration range. Switching between the two processes by varying the feedgas composition was strongly linked to the relative fluxes of the hydrogenic ions (H_2^+, H_3^+ and H^+) and the Ar^+-like ions (Ar^+ and ArH^+) in the plasma.

Pulsing the discharge turned out to be a useful tool to further modify the ion population at a given feedgas composition [10]. An increase of the hydrogenic ions with respect to the CW discharge was obtained with a low frequency modulation (<50 kHz), while a decrease of the Ar^+-like ion population was obtained. All these factors lead to structural modifications, reflected in the film Urbach energy values and the permeation properties of the a-C:H/PET system to He gas. This early work showed the importance of the film structure at atomic level over morphology for He permeation, in reference first to the above results and to a comparison between the carbon films and Al films grown in the same conditions on PET. It was observed that the surface of both films replicated the morphology of the pre-existing defects of the PET membranes. However, in spite of a surface defects similarity, the two kinds of material resulted in having different gas permeation properties.

This work was followed by new investigations, the results of which are now reported.

3.2. Determination of the film threshold thickness for full substrate coverage

Thin films are known to grow on a given substrate by different mechanisms that are dependent on the atom mobility on the substrate surface. The film continuity step can be reached in the very first instants of the substrate exposure to the vapour flux, as in the case of a layer-by-layer growth, or after a three-step process: nucleation and nuclei growth, later coalescence, and finally continuity. In any case, large intrinsic stress can develop in the growing film, characterizing each mechanism. So, stress measurements can be used as a fingerprint method for film growth studies [17, 18]. In particular, in the case of growth by a nucleation–coalescence–continuity mechanism, the generic observation is that the intrinsic stress evolves from compressive to tensile and then back to compressive, a behaviour referred to as CTC. The maximum tensile stress marks the full coverage step and can be employed to determine the threshold thickness value for full coverage. We applied these notions for the carbon films, grown directly on Si and on a polymer-like carbon pre-coated Si substrate. As already mentioned, the latter substrate was used to simulate the growth of the films on a plastic substrate such as PET. As the growth mechanism was investigated by means of stress measurements, the latter should be rigorously intrinsic to be related to the growth process. This could not be guaranteed with PET membranes. The polymer-like carbon pre-coating was 212 nm thick.

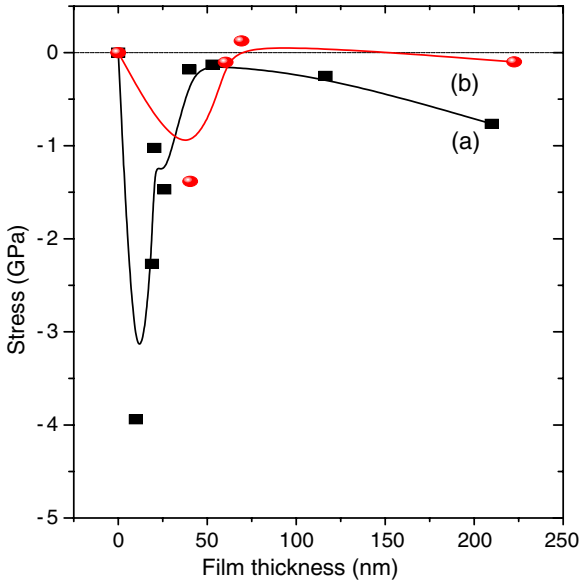

Figure 1. Compression–tension–compression (CTC) growth stress behaviour for a-C:H(16) films deposited on Si (curve a) and polymer-like carbon pre-coated Si (curve b).

Its polymer-like character was confirmed by a high electrical insulating character (not shown here), and a low nanohardness (∼1 GPa) relatively to the sputtered films (7–8 GPa for a-C:H ($x \neq 0$) and 16 GPa for a-C:H(0) [19]).

The residual stress was determined *ex situ* in a series of a-C:H(16) films with thickness increasing from ∼10 to ∼210 nm. Figure 1 shows its evolution during growth in a CW plasma, on Si (curve a) and on polymer-like carbon pre-coated Si (curve b). As is seen, both curves exhibit the CTC behaviour, indicating a nucleation–coalescence–continuity growth mechanism, with a full coverage stress measured in a 40–50 nm film on Si and a ∼70 nm film on the polymer. So we fixed the minimum thickness to the permeation tests of ∼60–70 nm.

3.3. Permeation properties

Generally speaking, in a heterogeneous system composed of a thin film deposited on a membrane (system named laminate hereafter) gas can permeate through the film in three ways: (i) gas flow through microscopic defects created in the film during its growth and handling such as pinholes or microcracks [4], (ii) transport through nanodefects such as nanochannels by a Knudsen-type diffusion mechanism [20], or (iii) transport in the solid state through the film's structural network. While in the two last cases the gas permeation rate, at a given temperature, depends on both the nature of the permeant (mass and/or size) and on the film thickness, permeation due to microdefects is independent of both parameters. It is a function only of the defect density and size in the film [4]. So one method to distinguish between the free-gas transport and the diffusional one (Knudsen or in the solid state) is by measuring the permeation rate as a function of the film thickness and checking the constancy of this parameter, provided the film thickness exceeds the threshold value for continuity. In figure 1 are reported the He permeation rates through the a-C:H/PET under study, with thicknesses from ∼65 to ∼250 nm. For comparison, the values from Al/PET are also shown. We found that the a-C:H/PET laminate behaved differently from Al/PET. In the first case, the permeation rate

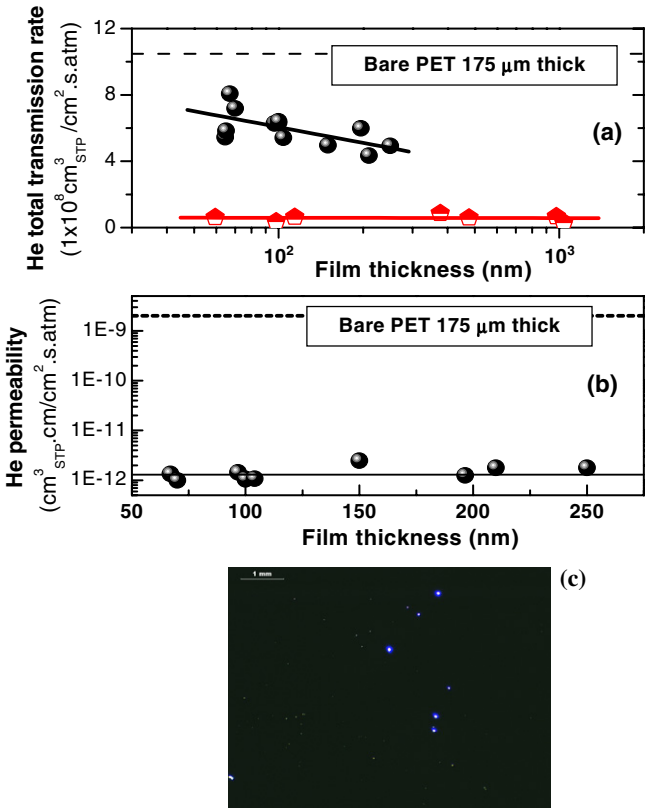

Figure 2. (a) Transmission rate of a-C:H(16)/PET and Al/PET laminates, upper and lower curve respectively as a function of the carbon film thickness and compared to the bare 175 μm thick PET substrate. (b) Intrinsic permeability of the a-C:H(16) films as a function of the film thickness and compared to the bare 175 μm thick PET substrate. (c) Surface optical micrograph of 1 μm Al film deposited on PET.

decreased when the thickness increased, while no such sensitivity was noticed for Al/PET. In the latter case it appears that permeation was biased by gas flow in the microdefects, while it is clear that He permeation through the a-C:H/PET laminates is governed by diffusion, though a specific mechanism (Knudsen or Fickian) needs to be defined. Besides, the surface examination of Al film revealed the presence of pinholes with dimensions ranging between ∼25 and 100 μm, as shown in figure 2(c) in a back illumination optical micrograph.

Let us recall that the Al films were grown with the same deposition apparatus and process as the C films and on PET substrates from the same commercial lot and cleaned with the same procedure prior to deposition. The experiment with Al/PET was useful in that the global laminate permeation rate due to microdefects in the film was derived and found to be in a ratio of 5.6×10^{-2} to that of a bare PET membrane. So it was possible to characterize our deposition system in terms of microdefect generation in the deposits on PET membranes. In fact, such defects are generally due to dust and asperities on the membrane surface, and to shadowing effects the latter can give rise to. Dust can be inherent to the deposition chamber environment, both inside and outside, and to the vacuum generation system. It can also collect on the plastic surface due to electrostatic charging.

By comparing the permeation rates obtained with a-C:H/PET and that due to microdefects on Al/PET, it is clear that a microdefect-biased gas transport would lead to much lower values

in a-C:H/PET than the measured ones. This fact and the dependence of the barrier efficiency on the film thickness indicate that gas transport through the film network and/or through nanoscale defects was by far the prevailing mechanism. It turns out that the film thickness in a-C:H/PET laminates is an important parameter for tailoring the global barrier improvement capabilities with respect to the bare PET. However, in order to properly characterize the gas barrier potentiality of such systems, one must determine the intrinsic permeability of the film material itself. Only in this manner can different a-C:H/PET laminates be compared within experiments or with literature data.

The intrinsic permeation properties of the films can be derived, in a first step, by considering the coated-PET system as an ideal laminate, neglecting the microdefects' contribution to the overall gas transport. A series resistance model (called the ideal laminate theory) is often applied to give the following relation between the permeability of the film (P), that of the PET membrane (P_{PET}) and the measured global permeability (P_{b}) of the film-PET laminate,

$$\frac{l_{\mathrm{b}}}{P_{\mathrm{b}}} = \frac{l_{\mathrm{f}}}{P} + \frac{l_{\mathrm{PET}}}{P_{\mathrm{PET}}}. \tag{3}$$

Here $l_{\mathrm{b}}, l_{\mathrm{f}}$ and l_{PET} are the whole film/PET, the single film and the single PET membrane thicknesses respectively. The values of the intrinsic permeability of the carbon films obtained from the above equation are displayed in figure 2(b) as a function of the film thickness, together with the P_{PET} value shown for comparison. As expected, the film permeability is practically constant over all the thickness range, with a mean value of $P = (1.295 \pm 0.54) \times 10^{-12}$ $\mathrm{cm}^3_{\mathrm{STP}}$ cm cm^{-2} s^{-1} atm^{-1}, i.e. in a ratio of 6.4×10^{-4} to P_{PET}.

As stressed above, here we took P_{b} equal to the permeability of an ideal laminate ($P_{\mathrm{b}} \equiv P_{\mathrm{IL}}$), justified by the fact that transport through microdefects was negligible with respect to the measured laminate permeability. Nonetheless, for a more rigorous determination of the intrinsic permeability of the carbon films, the transport through the microdefects should be taken into account too. P_{b} could then differ from P_{IL}, so the latter should be determined prior to applying equation (3). Roberts *et al* [3] developed a model for permeability for cases where this mechanism cannot be ignored. By using the finite-difference numerical method, they established the following relation:

$$P_{\mathrm{b}} = P_{\mathrm{d}} + \left(1 - \frac{P_{\mathrm{d}}}{P_{\mathrm{p}}}\right) P_{\mathrm{IL}} \tag{4}$$

where P_{p} is the bare polymer substrate permeability (here $P_{\mathrm{p}} = P_{\mathrm{PET}}$) and P_{d} is the permeability of the laminate due to the microdefects. In our case the permeability of the Al/PET system was taken as P_{d}. Due to the relatively low value of P_{d}, the application of equation (4) to calculate P_{IL}, then P, gave the same values as with equation (3). The a-C:H/PET system can therefore be considered as an ideal laminate system to a good approximation.

This way, we determined the intrinsic permeability of the films deposited in the whole range of plasma conditions obtained by varying either the feedgas composition or the modulation of the rf discharge (cf section 2.1). A survey of all the results obtained is displayed in figure 3(a) as film-to-PET intrinsic permeability ratios, for all the permeant gases. It can be seen that the film barrier properties can be lower by orders of magnitude than those of PET, in ratios down to the 10^{-4} range. The spectrum of the values for O_2 is poorer; those available are in a ratio to PET down to the 10^{-3} range.

Once the intrinsic permeability of the films was derived, a further step was to define the selectivity basis to the different gases, that is which of the molecular weight or the molecular size is the important factor. In fact, clarifying this aspect helped to further elucidate the permeation mechanism in the films. Transport of gas molecules by diffusion through a

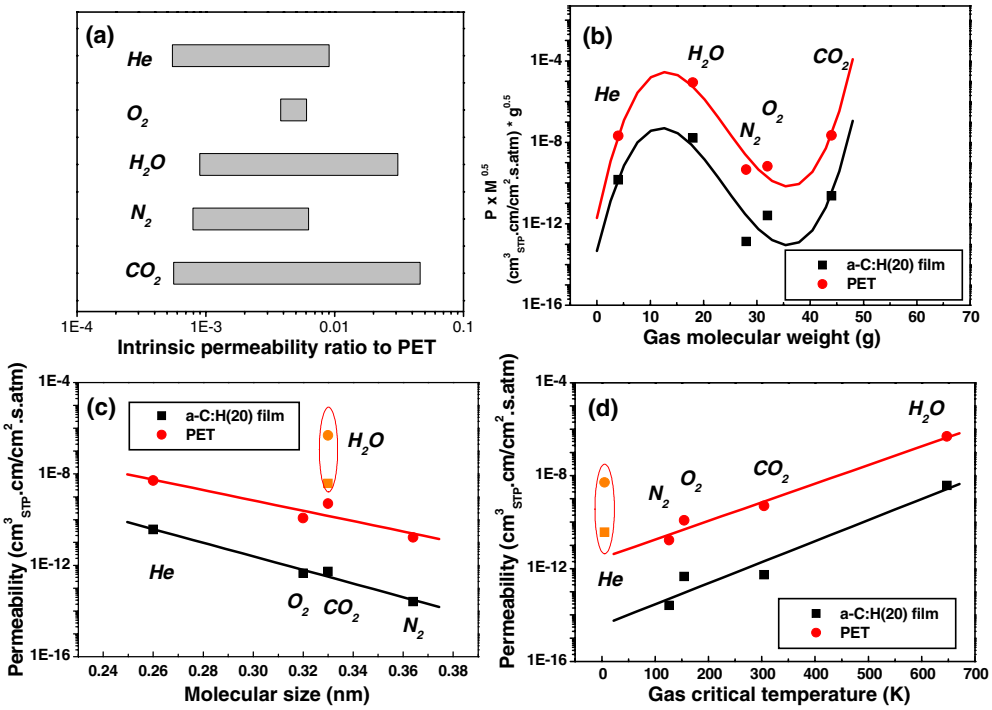

Figure 3. (a) Survey of a-C:H film barrier properties related to PET, in the whole experimental deposition parameter set, (b) $P \times M^{0.5}$ plot as a function of the gas molecular weight, M, within the Knudsen gas transport model (cf equation (5)), (c) intrinsic permeability versus the gas molecular size, (d) intrinsic permeability versus the gas critical temperature, for PET and a-C:H(20) film.

membrane can occur in ways depending on the nature of the interaction between the diffusing gas molecules and the membrane. Knudsen diffusion proceeds when the mean free path of the gas molecule diffusion is much larger than the defect size (nanopore, nanochannel). It proceeds in the gaseous state without the involvement of adsorption. In this regime the gas molecule passes through the nanodefect undergoing random collisions with the wall of the defect. The Knudsen permeability rate is given by

$$Q = (\eta d_{\mathrm{d}}/\tau \cdot l) \times (8/(9\pi MRT))^{1/2} \tag{5}$$

where η is the defect spatial density, d_{d} the defect size, τ the gas path tortuosity, M the gas molecular weight, T the temperature and R the gas constant. A characteristic feature of the Knudsen mechanism is that, for a given temperature and membrane thickness, $Ql(M)^{1/2} = P(M)^{1/2}$ remains constant as it depends only on the morphological properties of the membrane (η, d_{d} and τ).

We analysed the gas permeance of both the a-C:H films and the bare PET substrates within this model, as shown in figure 3(b). An a-C:H(20) film deposited in CW plasma was selected, as it was tested with all of the gases. The values of $P(M)^{1/2}$ were found to differ too much, by more than one order of magnitude, to be considered as constant over the He, CO_2, O_2, N_2 and H_2O gas series, either for the film or for PET. The permeance data did not fit the Knudsen model, which indicates that these gases do not permeate in the gaseous state. Solubility and solid-state diffusion must thus come into play in the gas permeation in these materials. The latter hypothesis is further supported by the dependence of the permeability

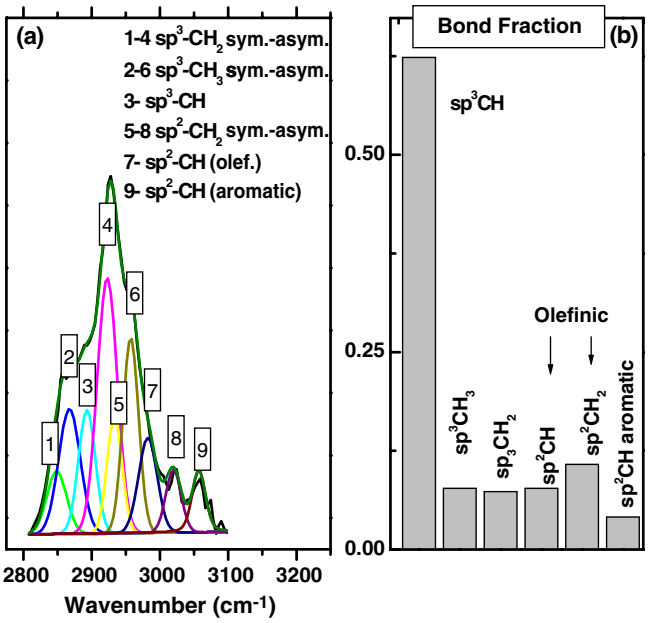

Figure 4. (a) $sp^i C–H_x$ stretch absorption spectrum ($i = 2, 3$ and $x = 1, 2, 3$) from an a-C:H(16) film deposited on Si; (b) bond fractions in the hydrogenated network.

on the gas molecular size. In figure 3(c) the intrinsic permeability of the a-C:H(20) film is plotted as a function of the gas molecular size, together with that of PET. Here we took a diameter value of 0.20 nm for He [21], 0.32 nm for O_2 [2], 0.33 nm for CO_2 [21], 0.36 nm for N_2 [22] and 0.33 nm for H_2O [2]. It turns out that, except for H_2O, the permeability scales inversely with the molecular size: $P(\mathrm{He}) > P(\mathrm{O_2}) \cong P(\mathrm{CO_2}) > P(\mathrm{N_2})$ while $\varnothing(\mathrm{He}) < \varnothing(\mathrm{O_2}) \cong \varnothing(\mathrm{CO_2}) < \varnothing(\mathrm{N_2})$, and this for both film and PET. Contrasting with this behaviour, the permeability scales directly with the gas critical temperature, as can be noticed in figure 3(d), excepting this time for He. So, the present results strongly suggest that He permeation is governed by diffusion, that of H_2O by solubility, and in that of O_2, CO_2 and N_2 both processes are prevailing. This interpretation is made on the basis of various models and correlation results reported in the literature. It has been established that diffusivity through an amorphous polymeric material relates well to the gas molecule size [23], while gas solubility is linked to various parameters all measuring the gas condensability: the gas critical temperature, the boiling point or the Lennard-Jones potential well depth (ε/k) [23–26]. The molecule size and diffusivity correlation stem from the fact that among the various factors which determine the diffusivity, the most important one is the free volume fraction of the host medium, actually the one accessible to the permeant molecules, thus depending on their own size.

3.4. Film structure

3.4.1. Film structure from the vibrational properties. A typical FT-IR transmittance spectrum, acquired from a 486 nm a-C:H(16) film deposited on Si in a CW discharge, is shown in figure 4(a). The band was deconvoluted, after a linear background subtraction, into individual peaks representing the specific stretching modes, namely: sp^3-CH, sp^3-CH_2, sp^3-CH_3, olefinic sp^2-CH, olefinic sp^2-CH_2 and aromatic sp^2-CH [13]. Whenever the modes are symmetric

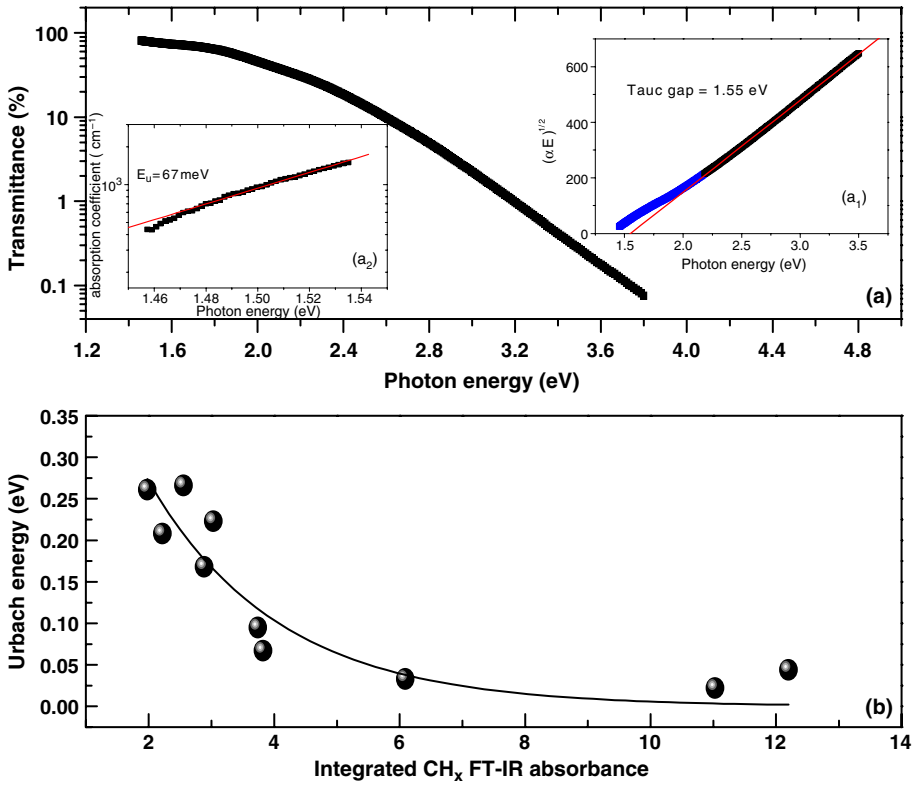

Figure 5. (a) Optical transmittance curve from a 486 nm thick a-C:H(16) film, deposited on 175 μm PET substrate. Insets a_1 and a_2: Tauc plot and Urbach fit of the sub-gap energy region respectively; (b) film hydrogen content effect on the Urbach energy.

(sym.) or anti-symmetric (asym.), it is indicated in the figure. With this deconvolution a chemical composition of the hydrogenated component of the films can be made in terms of relative amounts of the different sp^3-CH_x and sp^2-CH_y ($x = 1, 2$ or 3 and $y = 1$ or 2) if one takes into account the relative sensitivity factors, σ. Adopting the σ values given by Tanaka *et al* [27] for sp^3 $CH_{2,3}$, that for olefinic sp^2 CH used in [28] and that of aromatic sp^2 CH found in [29], i.e.

$$sp^3\ CH_3{:}sp^3\ CH_2{:}sp^3\ CH{:}sp^2\ CH\ \text{olefinic}{:}sp^2\ CH\ \text{aromatic} = 1{:}1.06{:}10{:}3.4{:}4,$$

the bond fractions in the hydrogenated component of the film structure were calculated. Olefinic sp^2 CH_2 and sp^2 CH were assumed to have the same σ. The results are shown in figure 4(b). Here, when a bond is characterized by two vibrational modes, only one is taken for the calculations (the asym. one for $sp^3CH_{2,3}$ bonds and the sym. one for the olefinic sp^2 CH_2).

It results that hydrogen appears mainly in terminating bonds with sp^3-carbon (sp^3-CH), itself involved in three-dimensional bondings with other carbons, which makes the hydrogenated amorphous phase of the films a rigid network rather than polymer-like.

3.4.2. Film structure from the optical properties. Figure 5(a) illustrates the transmittance curve obtained for a-C:H(16) film, as well as the Tauc and Urbach plots in the insets (a_1) and (a_2) respectively. A value of (1.55 ± 0.01) eV was obtained for E_g and (67 ± 10) meV for E_u. The structural implication of the optical gap and Urbach energies in a-C:H films is through

their relation to different kinds of disorder. The information is often sought in the light of existing models for amorphous semiconductors. In a-Si:H, as a typical example, the electron states can be divided into extended, band tails and deep states. Each of these originates from different physical processes: from long-range correlations and symmetry, structural disorder and structural defects respectively. In the case of the a-C:H films, the optical gap and band tail do not necessarily have the same physical origin as for a-Si:H as far as it is matter of structural disorder, but the two materials should be similar when it is matter of structural defects, as will discussed in the following sections.

The a-C:H film structure is complex and is generally modelled as a dispersion of two types of network, one made of sp^3 and the other of sp^2 C atoms, bound as C–C and C–H, with different spatial organizations. The optical gap arises from the π–π^* electron transitions, involving the sp^2 C sites, and is controlled both by the sp^2 C amount and cluster size and by the structural disorder in the clusters themselves [29]. This model can find some support, for instance in the work of Lonfat *et al*, who measured the energy gap of isolated carbon clusters as a function of their size [30]. Their results showed that for some clusters a dimension of $\sim$10 nm is sufficient to open the gap while others need a much lower value, $\sim$1 nm. Manifestly, beside the size effect, disorder and/or the chemical structure of the clusters may come into play.

Another kind of disorder which does not necessarily imply sp^2 C clustering is the one due to the sp^3 C clustering instead, embedded within the sp^2 graphite network [31]. Here the gap opening is due to distortions of the graphitic layers (puckering) which weaken the π-molecular orbital overlap.

So, defining a single or a prevailing structural cause of the presence of a gap in the a-C:H films seems hard. It is more likely that all are involved at different degrees.

As for the Urbach-edge absorption, its precise origin is not well known, despite its universal use to characterize 'disordered' systems. The reason is that it is related to a defect-induced disorder and the defects are not well-defined. Among those which can characterize the films, certainly the most important to take into consideration for gas barrier applications are the voids. In addition, the influence of the latter on the electron properties of amorphous semiconductors have been investigated with great interest. In a-Si:H their effects have been related to the generation of additional electron states, associated with the void surface, either in dangling bonds or in reconstructed molecular bonds. These defect states are believed to be distributed over the gap range. The transitions in which these states are involved are retained to give rise to the absorption tails [32], especially when dangling bonds lead to stable vacancy formation [33] with a consequent energy shift from deep states to tail states. Although the a-C:H materials differ strongly from the classical semiconductors by their electron hybridization peculiarity, it could however be interesting to compare the behaviour of the Urbach energy with the optical gap in our films with that in a-Si:H, reported in the literature. For amorphous a-Si:H, the Urbach energy shows a monotonic linear variation with the gap, a high gap corresponding to a low Urbach energy [35]. In order to check this kind of behaviour in the case of a-C:H films, we measured both parameters on various sets of films having different Tauc gap and Urbach values. The films resulted in having different dependence laws between these two parameters, as shown in figure 6(a). The E_u–E_g plot presents a non-monotonic variation of E_g as a function of E_u. Two regions can be distinguished in which the two parameters either are inversely proportional (region I) or scale directly (region II).

These results clearly indicate that (i) in a-C:H there is not a general rule for the interdependence of E_u and E_g and (ii) the two parameters reflect different kinds of disorder. This is further supported by their effect on the film density, as checked in figures 6(b) and (c), for films yielding imply the regions I and II defined in figure 6(a). For films in region I, the refractive index (here taken at a photon energy $E = 3$ eV) was taken as representative of the

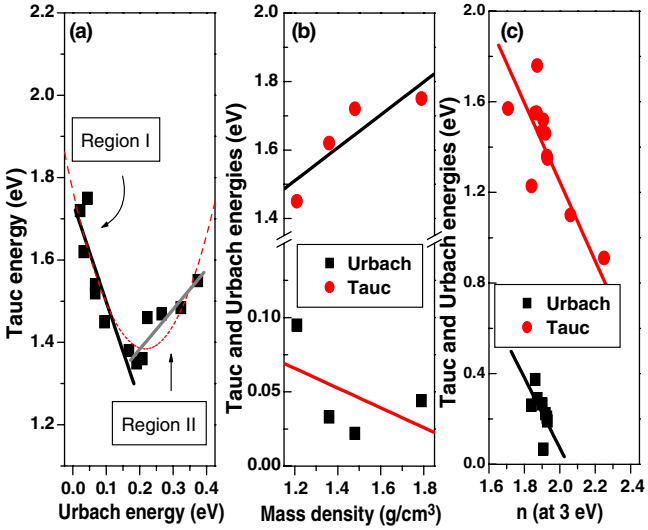

Figure 6. (a) Urbach energy—Tauc gap plot and its fit (solid lines) for the a-C:H films obtained with different (Ar–H_2) feedgas compositions. (b) Tauc and Urbach energies as a function of the film mass density in region (I) of the E_u–E_g curve in (a); (c) Tauc and Urbach energies as a function of the refractive index for films in region (II) of the E_u–E_g curve in (a).

film density [34], while for region II, E_u and E_g are plotted directly versus the mass density. For films in region I the highest density was obtained for the highest E_g, while for films in region II the trend was reversed. It is also worth noting that a common feature to all the films remains the effect of the Urbach energy: the highest density is found in the films with the lowest E_u over all the film series. This parameter measurement appears as a valuable tool to qualify the film compactness.

These findings lead us to distinguish between two kinds of disorder in our films: a structural disorder reflected in the Tauc gap energy and a defect disorder reflected in the Urbach energy. E_u, on the other hand, is strongly dependent on the hydrogen content of the films, i.e. on some aspects of the chemical structure of the latter. An exponential decrease of E_u upon the CH_x FT-IR integrated absorbance band was obtained, as shown in figure 5(b). This 'healing' effect of hydrogen has been encountered in classical amorphous semiconductors and seems to operate in the a-C:H films too.

3.5. Structural effects on the permeation properties of the films

In order to better understand the gas permeation mechanism through the films under study, correlations between the structural parameters defined previously and the permeability of the film material were searched for. From the permeation study results, it turned out that the dominant process in the gas transport through the films was by a solid-state process. In this case, permeation is the product of the gas diffusivity through the network (D) and the gas solubility in the network (S):$P = D \times S$ [36]. If diffusion is the limiting process for the barrier capability, the defect disorder level which affects the films can be of great influence. We looked for such an effect on the film intrinsic permeability, taking the Urbach energy as a measure of the defect disorder, as resulted from the previous section. The results are presented in figure 7(a). As expected, the higher E_u, the more favoured the He and CO_2 permeation (for N_2 the data are too few to make any conclusions about a trend). In contrast, no clear effect is

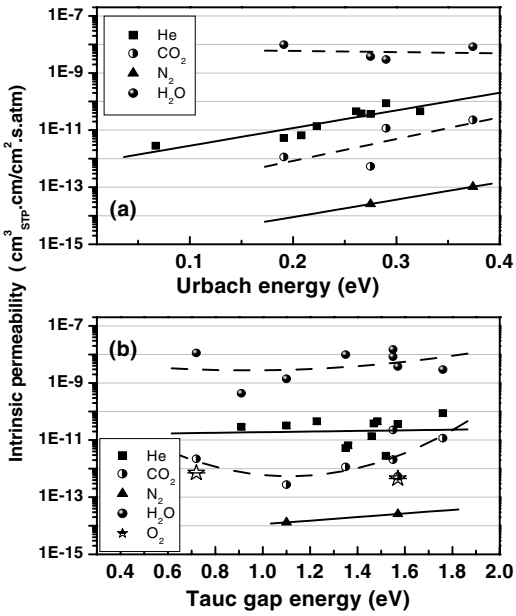

Figure 7. He, CO_2, O_2, N_2 and H_2O intrinsic permeability of a-C:H films as a function of (a) the Urbach energy, (b) the Tauc gap energy.

seen for H_2O, which permeates independently of E_u. Once again, the H_2O molecule exhibits a non-regular behaviour relatively to the other gases.

An effect of the structural disorder on the film permeability was also checked by plotting the intrinsic permeability for He, CO_2 and H_2O versus the Tauc gap (figure 7(b)). Contrarily to E_u, no neat dependence was observed: the data either manifest no significative sensitivity or are too scattered to show a neat trend. The film structural disorder seems of little effect on these gas transports.

So, excepting H_2O, the defect disorder level reflected in E_u remains the most valuable 'index' of gas permeability. In turn, the tight correlation of the permeation with the defect-induced optical properties of the material leads us to consider these defects as either open volumes by their very nature or involved in the formation of open volumes of such a low size to make the permeation kinetics sensitive to the gas molecular diameter value. It seems reasonable to define these open volumes as vacancies. Furthermore the results of the FT-IR analysis showed that hydrogen in the films was principally bound to sp^3 C sites, while the observed 'defect healing effect' of hydrogen concerned the sp^2 C sites. This suggests that the hydrogen effect on the film defects is probably indirect. Its presence is thought to prevent their formation rather than to 'heal' them. It more likely acts as a stress releaser at the junctions between the sp^3 and sp^2 C domains where otherwise network relaxation occurs by forming dangling bonds, precursors of vacancies. H is able to replace by terminal C–H bonds those strained sp^3 C–sp^2 C or sp^3 C–sp^3 C bonds.

4. Summary

Intrinsic gas barrier and structural properties of a-C:H films deposited on PET substrates were studied. Carrying out permeation tests with gases differing by their molecular mass and diameter allowed us to discriminate between the various possible permeation mechanisms:

gas flow through microscopic defects, Knudsen diffusion through nanodefects or solubility–diffusion based permeation. A decreasing He transmission rate with the film thickness, a non-fitting of the Knudsen model by the intrinsic permeability, and an inverse scaling of the latter with the gas molecular size, all indicate a solubility–diffusion mechanism. Unlike the other gases, H_2O vapour showed a non-characteristic behaviour. Its permeation seems to be governed by solubility, in contrast with that of He which is favoured by diffusion. For a better understanding of the permeation characteristics, a correlation between the latter and the film structure helped to define a structural parameter, represented by the Urbach energy, as a permeability index for the films. This parameter was principally related to the hydrogenation state of the films.

Acknowledgments

This work was supported by PAT (Fondo Progetti Ricerca, Trento, Italy). Thanks are due to P Chiggiato from CERN of Geneva for helpful discussions, and M Bianchi, G Coser and V Micheli for technical assistance.

References

[1] Erlat A G, Henry B M, Ingram J J, Mountain D B, McGuigan A, Howson R P, Grovenor C R M, Briggs G A D and Tsukahara Y 2001 *Thin Solid Films* **388** 78
[2] Roberts A P, Henry B M, Sutton A P, Grovernor C R M, Briggs G A D, Miyamoto T, Kano M, Tsukahara Y and Yanaka M 2002 *J. Membr. Sci.* **208** 75
[3] Iwamori S, Gotoh Y and Moorthi K 2003 *Vacuum* **68** 113
[4] Chatham H 1996 *Surf. Coat. Technol.* **78** 1
[5] Moser E M, Urech R, Hack E, Künzli H and Muller E 1998 *Thin Solid Films* **317** 388
[6] Vasquez-Borucki S, Jacob W and Achete C A 2000 *Diamond Relat. Mater.* **9** 1971
[7] Camargo S S, Damasceno J C and Beyer W 2002 *Diamond Relat. Mater.* **11** 1091
[8] Zhu P, Teranishi M, Xiang J, Masuda Y, Seo W-S and Koumoto K 2005 *Thin Solid Films* **473** 351
[9] Abbas G A, Roy S S, Papakonstantinou P and McLaughlin J A 2005 *Carbon* **43** 303
[10] Laidani N, Bartali R, Anderle M, Chiggiato P and Chuste G 2005 *Diamond Relat. Mater.* **14** 1023
[11] Laidani N, Bartali R, Tosi P and Anderle M 2004 *J. Phys. D: Appl. Phys.* **37** 2593
[12] Colthup N B, Daly L H and Wiberley S E 1969 *Introduction to Infrared and Raman Spectroscopies* (New York: Academic)
[13] Brodsky M H, Cardona M and Cuomo J J 1977 *Phys. Rev.* B **16** 3556
[14] Tauc J 1970 *Mater. Res. Bull.* **5** 721
[15] Sagnes E, Szurmak J, Manage D and Zukotynski S 1999 *J. Non-Cryst. Solids* **249** 69
[16] Heavens O S 1970 *Thin Film Physics* (London: Methuen & CO)
[17] Spaepen F 2000 *Acta Mater.* **48** 31
[18] Floro J A, Hearne S J, Hunter J A, Kotula P, Chason E, Seel S C and Thompson C V 2001 *J. Appl. Phys.* **89** 4886
[19] Brusa R S, Macchi C, Mariazzi S, Karwasz G P, Laidani N, Bartali R and Anderle M 2005 *Appl. Phys. Lett.* **86** 221906
[20] Knudsen M 1909 *Ann. Phys.* **28** 75
[21] Lee D and Oyama S T 2002 *J. Membr. Sci.* **210** 291
[22] Ayale D, Lozano A E, De Abajo J, Garcia-Perez C, de la Campa J G, Peinemann K-V, Freeman B D and Prabhakar R 2003 *J. Membr. Sci.* **215** 61
[23] Fried J R and Ren P 2000 *Comput. Theor. Polym. Sci.* **10** 447
[24] Shah V M, Hardy B J and Stern S A 1986 *J. Polym. Sci.* B **24** 2033
[25] Masuda T, Iguchi Y, Tang B-Z and Higashimura T 1988 *Polymer* **29** 2041
[26] El-Hibri M J and Paul D R 1986 *J. Appl. Polym. Sci.* **31** 2533
[27] Tanaka M, Iwata Y, Fujimoto F, Komaki K, Kobayashi K, Yamashita H and Haba M 1990 *Nucl. Instrum. Methods Phys. Res.* B **45** 223
[28] Gielen J W A M, Kleusken P R M, van de Sanden M C M, Dekempeneer E H A and Meneve J 1996 *J. Appl. Phys.* **80** 5986

[29] Robertson J 2002 *Mater. Sci. Eng.* R **37** 129
[30] Lonfat M, Marsen B and Sattler K 1999 *Chem. Phys. Lett.* **313** 539
[31] Gotoh Y 1997 *J. Nucl. Mater.* **248** 46
[32] Connel G A N Optical properties of amorphous semiconductors *Springer Topics in Applied Physics, Amorphous Semiconductor* vol 36, ed M H Brodsky (Berlin: Springer) pp 73–109
[33] Miranda C R, Antonelli A, da Silva A J R and Fazzio A 2004 *J. Non-Cryst. Solids* **338–340** 400
[34] Schawrtz-Sellinger T, von Keudell A and Jacob W 1999 *J. Appl. Phys.* **86** 3968
[35] Panwar O S, Mukherjee C and Bhattacharyya R 1999 *Sol. Energy Mater. Sol. Cells* **57** 373 and references therein
[36] Crank J 1975 *The Mathematics of Diffusion* 2nd edn (London: Clarendon, Oxford University Press) chapter 4, pp 44–68